ACS APPLIED MATERIALS & INTERFACES

www.acsami.org

Research Article

Antiperovskite Oxides as Promising Candidates for High-Performance Ferroelectric Photovoltaics: First-Principles Investigation on Ba_4As_2O and Ba_4Sb_2O

Youngho Kang* and Seungwu Han

Cite This: *ACS Appl. Mater. Interfaces* 2020, 12, 43798−43804

Read Online

ACCESS | Metrics & More | Article Recommendations | Supporting Information

ABSTRACT: Owing to polarization-driven efficient charge carrier separation, ferroelectric semiconductors with narrow band gaps (~1.3 eV) can constitute an ideal active layer for photovoltaics (PVs), as demonstrated in recent studies on lead halide perovskite solar cells. In this study, antiperovskite oxides with a composition of Ba_4Pn_2O (Pn = As or Sb) are proposed as promising candidates for high-performance ferroelectric PVs. Using density functional theory calculations, it is revealed that Ba_4Pn_2O exhibits moderate macroscopic polarization enough for charge carrier separation. Moreover, they are predicted to have direct band gaps close to the optimal Shockley−Queisser value. By investigating optical absorption coefficients and resulting short-circuit currents, it is demonstrated that a very thin layer of Ba_4Pn_2O can yield large photocurrents. The effective masses of charge carriers in Ba_4Pn_2O are found to be fairly small (<0.2m_e), implying facile extraction of photocarriers. The favorable simulation results along with the confirmed synthesizability of the materials strongly suggest that Ba_4Pn_2O will be an active layer suitable for PVs.

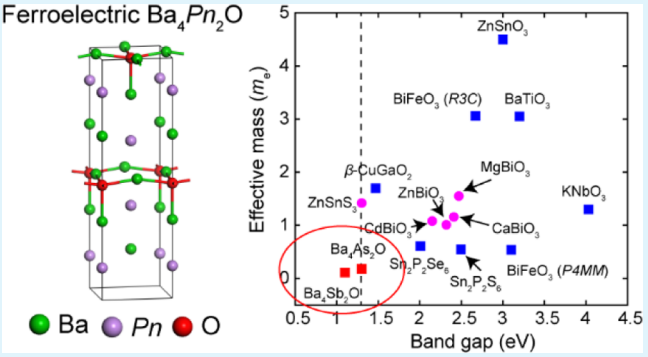

KEYWORDS: *photovoltaics, photoabsorber, oxide, ferroelectricity, density functional theory*

1. INTRODUCTION

Ferroelectrics are a class of materials that are characterized by spontaneous electric polarizations that arise from the broken inversion symmetry of the crystallographic unit cell.[1−3] Because the electric polarization facilitates the separation of photoexcited e−h pairs, ferroelectric materials that possess a small band gap for absorbing a large portion of solar spectrum can constitute promising active layers for photovoltaic (PV) devices. However, most of the known ferroelectric materials such as ferroelectric oxides with a perovskite structure, that is, ABO_3, exhibit unfavorably large band gaps (>2.5 eV).[3−7] As such, they can only convert a small part of light in the solar spectrum to electricity, resulting in power conversion efficiencies (PCEs) less than 1%. For instance, thin films of ferroelectric $BiFeO_3$ with a band gap of 2.67 eV have been widely studied for PV applications, but they can absorb only 20% of the solar spectrum, resulting in low PCEs (~0.24%).[8,9]

To resolve the limitation mentioned above, many efforts have been made to tune the band gap of known ferroelectric materials via structural and chemical modifications or exploring new chemical compositions. Consequently, several ferroelectric materials such as Bi_2FeCrO_6 (BFCO),[2] $[KNbO_3]_{1-x}[BaNi_{1/2}Nb_{1/2}O_{3-\delta}]_x$,[10] and $LuMnO_3$[11] were synthesized with band gaps below 2 eV. However, solar cells incorporating these materials still lag in performance compared to conventional p−n junction solar cells based on Si and GaAs. This is partly attributed to the localized nature of charge carriers in those ferroelectric materials with effective masses larger than 1m_e, which limits amplification of photocurrents.[12,13] For example, BFCO has a band gap of 1.4 eV, close to the optimal Shockley−Queisser value, but a short-circuit current of single-layer BFCO PV cells recorded 10 mA/cm^2 that is only one-third of those using GaAs with a similar band gap (1.42 eV).[2] As a result, PCEs of BFCO solar cells were below 3.3%, which is far smaller than that of single-crystalline GaAs solar cells (29%). Like BFCO, a solar cell using $LuMnO_3$ with a band gap of 1.48 eV was reported to show a very low photocurrent density of 0.52 mA/cm^2, yielding only 0.11% PCE.[11]

Recently, lead halide perovskites (LHPs) such as $CH_3NH_3PbI_3$ (MAPI) have received significant attention because of high PCEs over 20%.[14,15] While a narrow band

Received: July 19, 2020
Accepted: September 8, 2020
Published: September 8, 2020

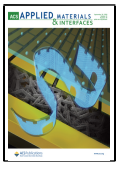

https://dx.doi.org/10.1021/acsami.0c13034
ACS Appl. Mater. Interfaces 2020, 12, 43798−43804

gap (~1.6 eV) and small effective masses of charge carriers are primary reasons for the high PCEs, spontaneous electric polarizations from organic species (such as CH_3NH_3) with permanent dipoles are also thought to be important.[16,17] However, LHPs suffer from instabilities related to organic components, which impedes their practical applications.[18,19]

In this work, we propose fully inorganic antiperovskite oxides with a composition of Ba_4Pn_2O (Pn = As or Sb) as promising candidates for high-performance ferroelectric PVs. These materials were reported to have proper band gaps for PV applications in a previous high-throughput computational study.[20] The present density functional theory (DFT) calculations indicate that Ba_4Pn_2O exhibits macroscopic polarizations of ~11 $\mu C/cm^2$, which would be enough for charge separation.[11] Furthermore, from many-body quantum-mechanical calculations, Ba_4As_2O and Ba_4Sb_2O are predicted to have direct band gaps of 1.1 and 1.3 eV, respectively, which are close to the optimal Shockley–Queisser value (1.3 eV).[21] By calculating short-circuit currents, we also demonstrate that a very thin layer of Ba_4Pn_2O can yield substantial photocurrents because of high absorption coefficients. We also find the effective masses of charge carriers in Ba_4Pn_2O to be fairly small. Thus, facile extraction of photocarriers is expected when these materials are applied to actual devices. The favorable simulation results, together with the confirmed synthesizability of the materials, suggest that Ba_4Pn_2O holds great potentials as active layers for PVs.

2. METHODOLOGY

2.1. DFT Calculations. All the DFT calculations were carried out using Vienna Ab initio Simulation Package code with the projector augmented wave pseudopotentials.[22,23] The kinetic energy cutoff of 500 eV was used for expanding the plane-wave basis and a 4 × 4 × 6 Γ-centered *k*-point grid was selected for the Brillouin zone (BZ) sampling. The crystal structure was fully relaxed until the forces acting on every atom become less than −0.005 eV/Å. The vibrational spectrum was obtained using the frozen-phonon method with the 2 × 2 × 2 supercell. The anharmonic interatomic force constants (IFCs) up to the sixth order were calculated using the compressive sensing lattice dynamics method, as implemented in the ALAMODE package.[24,25] To this end, we sampled 40 configurations with different atomic displacements from the trajectory of ab initio molecular dynamics at 500 K. The forces acting on each atom were computed for the selected geometries and they were fitted by the Taylor expansion potential to extract the IFCs. For the *GW* calculations, the initial wave functions and eigenvalues were obtained using Perdew–Burke–Ernzerhof (PBE)[26] calculations and a 4 × 4 × 6 Γ-centered *k*-point grid and 360 bands were employed to compute the self-energies. These parameters ensured the convergence of the quasiparticle gap within 0.1 eV (the convergence tests are present in Figure S1).

2.2. Optical Absorption Coefficient. To obtain the optical absorption spectrum in Figure 5a, we initially evaluated the imaginary part of dielectric functions (ϵ_2) within the independent particle approximation using PBE with spin–orbit coupling (SOC) calculations and the real part (ϵ_1) was obtained by the Kramers–Kronig transformation of ϵ_2. The optical absorption coefficient was then computed as follows

$$\alpha_{ij} = \frac{2\omega}{c}\sqrt{\frac{\sqrt{\epsilon_{1,ij}{}^2 + \epsilon_{2,ij}{}^2} - \epsilon_{1,ij}}{2}} \quad (1)$$

where c is the speed of light and i and j denote the Cartesian axis. By applying the scissor operator, we rigidly shifted the calculated absorption spectrum of Ba_4Pn_2O to match the band gap obtained from the *GW* method. This scissor operator approximation was validated in a previous work.[27]

For calculating the absorption coefficient of a polycrystalline material (α_{poly}), we evaluated the dielectric function for the polycrystal (ε_{poly}) based on the effective medium theory[28]

$$\frac{\varepsilon_{xx} - \varepsilon_{poly}}{\varepsilon_{xx} + 2\varepsilon_{poly}} + \frac{\varepsilon_{yy} - \varepsilon_{poly}}{\varepsilon_{yy} + 2\varepsilon_{poly}} + \frac{\varepsilon_{zz} - \varepsilon_{poly}}{\varepsilon_{zz} + 2\varepsilon_{poly}} = 0 \quad (2)$$

In tetragonal Ba_4Pn_2O, $\varepsilon_{xx} = \varepsilon_{yy} = \varepsilon_\perp$ and $\varepsilon_{zz} = \varepsilon_\parallel$. Thus, eq 2 is reduced to $\varepsilon_{poly} = 0.25(\varepsilon_\perp + \sqrt{\varepsilon_\perp{}^2 + 8\varepsilon_\perp\varepsilon_\parallel})$.

3. RESULTS AND DISCUSSION

In previous experiments, Ba_4Pn_2O was synthesized through reaction of constituting elements in corundum crucibles or tantalum tube under an argon atmosphere at elevated temperatures.[29,30] From the analysis of powder X-ray diffraction pattern at room temperatures, they were reported to crystallize in antiperovskite-derived tetragonal structures (Figure 1a), wherein the anion and cation positions are

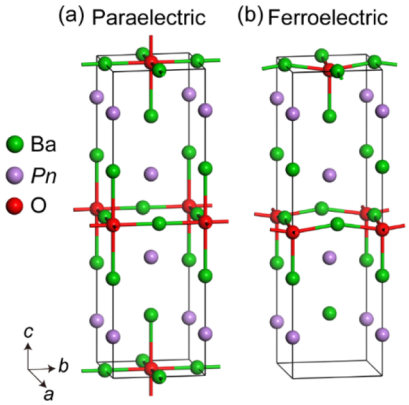

Figure 1. Atomic structures of Ba_4Pn_2O in (a) paraelectric and (b) ferroelectric phases.

switched in comparison to the perovskite structure. This structure is the layered antiperovskite that has the chemical formula A_2BX_4, where A = Pn, B = O, and X = Ba. In this antiperovskite structure, each O atom is surrounded by six Ba atoms, forming an octahedral group (OBa_6), and Pn atoms occupy the corner of the cube. The space group of this reported structure is *I*4/*mmm* and includes the inversion symmetry, and therefore, it is a paraelectric phase.

We note that the powder diffraction analysis may be difficult to precisely identify the presence of small distortions in the atomic structure such as a low-angle tilting of octahedral units or a ferroelectric displacement.[31,32] Therefore, to confirm whether the given crystal structure is the most stable, we calculate in Figure 2a,b phonon dispersions of Ba_4Pn_2O under the reported crystal symmetry (*I*4/*mmm*). The lattice parameters and internal coordinates are fully relaxed at 0 K within the PBEsol functional[33] that is known to accurately produce structural parameters of solids. It is found in both

https://dx.doi.org/10.1021/acsami.0c13034
ACS Appl. Mater. Interfaces 2020, 12, 43798–43804

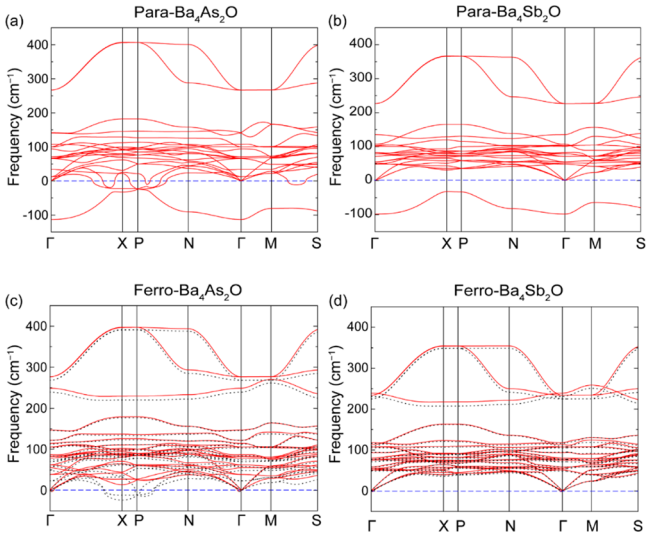

Figure 2. Phonon dispersions of (a) Ba_4As_2O and (b) Ba_4Sb_2O in paraelectric phase at 0 K. Phonon dispersions of (c) Ba_4As_2O and (d) Ba_4Sb_2O in ferroelectric phase at 0 K (black dashed lines) and 300 K (red solid lines).

materials that unstable optical modes exist at different high-symmetry points in the BZ, indicating that the reported crystal structure is not the ground state. In particular, the magnitude of the imaginary frequency of the soft modes is pronounced at the BZ center. This implies that a ferroelectric distortion can lower the energy of the Ba_4Pn_2O crystals most significantly. To identify the ground-state structure, we compute the total energy of Ba_4Pn_2O as a function of the displacement amplitude of the unstable mode at Γ, Q_Γ, which shows that both materials display double-well-type energy surfaces (Figure 3a,b). In the minimum energy structures (Figure 1b), the O^{2-} ion is off-centered in one direction along the *c*-axis, while the two axial Ba^{4+} ions are displaced in the opposite direction, lifting the inversion symmetry. As a result, a finite electric polarization can exist in the new minimum structure. We find that Ba_4As_2O and Ba_4Sb_2O are more stable in the ferroelectric phase than in

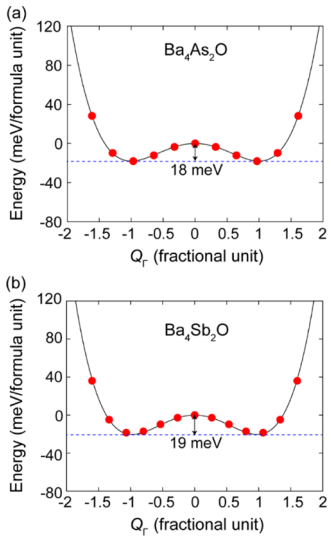

Figure 3. Calculated total energy of (a) Ba_4As_2O and (b) Ba_4Sb_2O as a function of the displacement amplitude of the unstable mode at Γ, Q_Γ.

the paraelectric phase by 18 and 19 meV/f.u., respectively. A full relaxation of the lattice and ion coordination does not affect the tetragonal shape of the crystal structure of Ba_4Pn_2O but increases the energy differences to 40 and 43 meV/f.u. for Pn = As and Sb, respectively. Note that the imaginary mode at the N and M points leads to antiferroelectric phases based on a monoclinic ($C2/m$) and a tetragonal ($P4/nmm$) phase, respectively, which are less stable than the ferroelectric phase (see Figures S2a,b).

The black dashed lines in Figure 2c,d are phonon dispersion curves for the (volume relaxed) ferroelectric phases at 0 K, which clearly shows that the unstable mode at the zone center disappears in the ferroelectric Ba_4Pn_2O. However, in contrast to Ba_4Sb_2O, soft modes appear at the X and P points in Ba_4As_2O, implying that this phase is still unstable at low temperatures (see Figure S2c). To check whether the ferroelectric phase of Ba_4As_2O can be stabilized at elevated temperatures by anharmonic phonon−phonon interactions, we calculate the phonon spectrum at 300 K by considering anharmonicity in interatomic force constants. The results are presented as red solid lines in Figure 2c, showing that all the phonon modes in Ba_4As_2O become stabilized. On the other hand, phonon dispersions of Ba_4Sb_2O at 300 K remain similar to those at 0 K, as shown in Figure 2d. As such, while the ferroelectric structure of Ba_4As_2O is unstable at 0 K, our results show that both Ba_4As_2O and Ba_4Sb_2O can exist in the ferroelectric phase at room temperatures. In Table 1, we

Table 1. Lattice Parameters of Ba_4Pn_2O in the Paraelectric and Ferroelectric Phases[a]

	Ba_4As_2O		Ba_4Sb_2O	
	Para	ferro	para	ferro
a (c5)	5.15	5.10 (5.11)	5.25	5.21 (5.23)
c (c5)	17.13	17.44 (17.46)	18.09	18.44 (18.36)
ΔP ($\mu C/cm^2$)		11.38		11.54

[a]The experimental lattice parameters[30] are provided in the parenthesis. ΔP is the macroscopic polarization.

compare the calculated lattice parameters of Ba_4Pn_2O in the paraelectric and ferroelectric phases with experiments and find that the values for the ferroelectric phases are in better agreement with the experimental data. (Another experiment[29] reported smaller lattice parameters for Ba_4As_2O compared to those presented in Table 1, but we confirmed that considering such smaller lattice parameters does not affect our conclusion, namely, the ferroelectric phase is favored over the paraelectric phase energetically.)

To examine the optical properties of Ba_4Pn_2O, we calculate the band structure using the PBE functional. The calculations include SOC, which reduces the band gap of Ba_4As_2O and Ba_4Sb_2O by 0.10 and 0.23 eV, respectively, lifting the degeneracy at the valence band maximum (Table 2). (For PBE + SOC calculation, we employ the same energy cutoff and k-point grid as those for PBEsol calculations. These computational parameters ensure satisfactory convergence of the band gap, as shown in Table S1.) We then carry out *GW* calculations to evaluate the accurate band gaps of Ba_4Pn_2O. Among various levels of self-consistency, we adopt the GW_0 scheme in which eigenvalues are updated for Green's function (G), while the screened Coulomb potential (W) is fixed to the initial DFT result. This approach could reproduce experimental band gaps of diverse semiconductors with high accuracies.[34,35] In

https://dx.doi.org/10.1021/acsami.0c13034
ACS Appl. Mater. Interfaces 2020, 12, 43798−43804

Table 2. Band Gap (in eV) of Ba_4Pn_2O Calculated Using Various Computational Methods[a]

	Ba_4As_2O	Ba_4Sb_2O
PBE	0.59	0.59
PBE + SOC	0.49	0.36
GW_0 + SOC	1.30	1.10

[a]In the GW_0 + SOC values, the SOC effect is assumed to be the same as that of the PBE calculations.

addition, to reduce computational cost, we assume that SOC affects the band structure as in the PBE calculations and rigidly shifts the band structure by the same amount as in PBE, omitting the SOC term in the GW_0 calculations. Figure 4

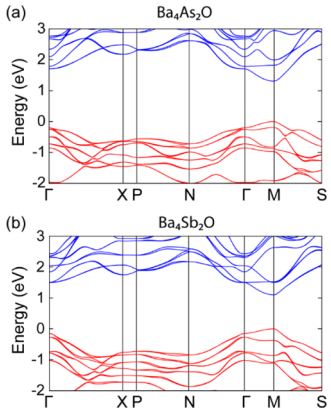

Figure 4. Band structure of (a) Ba_4As_2O and (b) Ba_4Sb_2O in the ferroelectric phase obtained using PBE + SOC calculations. Valence band maximum is set to 0 and the conduction bands rigidly shift for the band gap to match the GW_0 + SOC value (see text).

displays the PBE band structures of Ba_4Pn_2O in which the conduction bands rigidly shift for the band gap to match the GW_0 + SOC values. It is noticeable that Ba_4Pn_2O has a direct band gap at the M point, and therefore, the strong band edge absorption is expected. From the GW_0 + SOC calculations, the direct band gaps are predicted to be ∼1.30 and ∼1.10 eV for Ba_4As_2O and Ba_4Sb_2O, respectively. These band gaps are close to the optimal Shockley−Queisser value (∼1.3 eV).

Based on the electronic band structures in Figure 4, we calculate the optical absorption coefficient (α) as a function of the photon energy for Ba_4Pn_2O (Figure 5a). Because of the tetragonal symmetry, the α is distinct between in-plane ($\alpha_\perp$) and out-of-plane ($\alpha_\parallel$) directions (Figure S3). In actual applications, thin films of active layers are likely to be synthesized in a polycrystalline form. Thus, we present, in Figure 5a, α for the polycrystalline phase α_{poly}, that is obtained by the effective medium theory in which the polycrystalline system is regarded as an isotropic dielectric medium.[28] We find that the α_{poly} of Ba_4Pn_2O starts to rise at their band gaps and rapidly increases above 10^4 cm^{-1} for photons within the visible range (2.0−3.0 eV). Therefore, their absorption properties are promising for PV applications. The higher value of α_{poly} in Ba_4Sb_2O than Ba_4As_2O is ascribed to the smaller band gap of Ba_4Sb_2O. The advantage of Ba_4Pn_2O is more evident when compared to those of MAPI and Si (Figure 5a), which shows that Ba_4Pn_2O absorbs visible light more efficiently than MAPI with a direct band gap of ∼1.6 eV. Meanwhile, Si poorly absorbs visible light compared to the other materials because

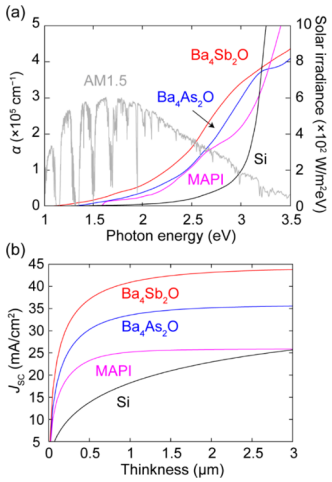

Figure 5. (a) Optical absorption coefficients as a function of photon energy for Ba_4Pn_2O, MAPI, and Si. Experimental data for MAPI and Si are adopted from ref 36. The gray line indicates the AM1.5 solar irradiance. (b) Short-circuit current (J_{SC}) with respect to a film thickness for Ba_4Pn_2O, MAPI, and Si.

of the indirect nature of the band gap, although the band gap is sufficiently narrow (∼1.1 eV).

We point out that low absorption coefficients as in Si do not necessarily mean low PCEs; the highest PCE of Si solar cells actually exceeds 20%.[16] However, to achieve such high PCEs, the active layer with low absorption coefficients should be thick enough to absorb solar spectrum completely (see our discussion below). As a result, Si is not used in thin-film solar cells. Furthermore, increasing the thickness of the active layer would raise the cost of solar cells and degrade the PCE because of enhanced nonradiative recombination.[19]

To produce photocurrents, photocarriers generated in the active layer should reach the nearby electrodes. Therefore, it is desirable to make the active layer as thin as possible. Furthermore, thinner active layers reduce costs and allow for flexible solar cells.[17] Owing to higher absorption coefficients, Ba_4Pn_2O films can be thinner than MAPI and Si with similar efficiencies. We explicitly demonstrate this benefit of Ba_4Pn_2O by evaluating the short-circuit current (J_{SC}) as a function of film thickness (d):

$$J_{SC}(d) = e\int_{\omega_g}^{\infty} \frac{\mathrm{AM1.5G}(\omega) \times (1 - \mathrm{e}^{-\alpha d})}{\hbar\omega}\, \mathrm{d}\omega \quad (3)$$

where e is the electron charge, AM1.5G is the solar spectrum of Air Mass 1.5 Global (Figure 5a), $\hbar$ is the Planck constant, and ω is the photon frequency. In this formula, the internal quantum efficiency is assumed to be 1, namely, all the photons absorbed by an active layer contribute to the current. Figure 5b shows that the J_{SC}'s of the direct gap semiconductors Ba_4Pn_2O and MAPI rapidly grow with d and almost reach the maximum even at d < 1 μm. However, we find that Ba_4Pn_2O yields higher J_{SC}'s than for MAPI at any d owing to the higher absorption coefficients. On the other hand, the J_{SC} for Si increases relatively slowly with respect to d and remains lower than that of MAPI until its thickness is ∼3 μm.

Next, we examine the charge transport property by evaluating effective masses of electron (m_e^*) and hole (m_h^*) of Ba_4Pn_2O (Table 3). We obtain the effective masses using HSE06 hybrid functionals[37,38] that accurately describe the band dispersion of semiconductors.[39,40] Like the absorption

https://dx.doi.org/10.1021/acsami.0c13034
ACS Appl. Mater. Interfaces 2020, 12, 43798−43804

Table 3. Effective Masses (in m_e) of Ba_4Pn_2O Calculated Using the HSE06 + SOC Method

	Ba_4As_2O		Ba_4Sb_2O	
	[001]	[100]	[001]	[100]
m_e^*	0.75	0.18	0.75	0.12
m_h^*	1.3	0.14	1.67	0.10

coefficients, the effective mass depends on the crystal axis in Ba_4Pn_2O. We find that both electron and hole have smaller effective masses along the in-plane direction ([100]) than the out-of-plane direction ([001]). This occurs because the outermost p_x and p_y states of Pn ($d_{x^2-y^2}$ states of Ba) that are major constituents of valence (conduction) bands (Figure S4) overlap each other along the in-plane direction more efficiently than the out-of-plane direction. On the other hand, the lighter effective masses along the in-plane direction indicates that a fast diffusion path to electrodes for charge carriers in polycrystalline films can always be formed by interconnecting the in-plane direction of different grains.[28] Thus, together with the ferroelectricity, the good transport property of Ba_4Pn_2O will allow for facile extraction of photocarriers.

To highlight the promise of Ba_4Pn_2O in PV applications, we compare in Figure 6 the carrier effective masses and optical

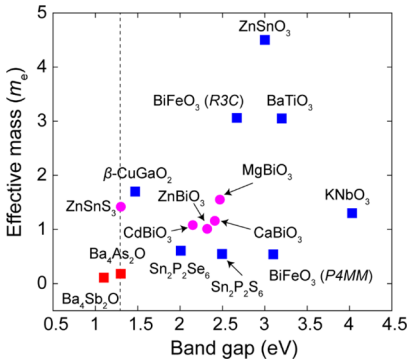

Figure 6. Band gap energy and effective mass of various ferroelectric semiconductors. Red squares denote the data for Ba_4Pn_2O, blue squares for synthesized materials (β-$CuGaO_2$,[12,43] $BiFeO_3$,[5,44] $KNbO_3$,[7,45] $BaTiO_3$,[6,46] $ZnSnO_3$,[42] $Sn_2P_2Se_6$, and $Sn_2P_2S_6$[47]), and purple circles for theoretically suggested materials [$ZnSnS_3$[42] and $ABiO_3$ (A = Cd, Zn, Ca, and Mg).[41] The vertical dashed line indicates the Shockley–Queisser value of the band gap.

(direct) band gaps, two critical properties, among known ferroelectric semiconductors and Ba_4Pn_2O. Only the larger value between m_e^* and m_h^* is presented because slower carriers limit the solar cell performance. When the effective mass tensor is anisotropic, we select the lowest one because the corresponding direction may form low-resistance paths in polycrystalline films. Figure 6 confirms that only Ba_4Pn_2O possesses both favorable band gaps close to the Shockley–Queisser value and low effective masses ($<0.2m_e$) (see red squares). Most of the known ferroelectric materials that were experimentally synthesized (blue squares) have wider band gaps (>2.5 eV) than those of Ba_4Pn_2O. Furthermore, these materials exhibit heavy effective masses ($>1m_e$), implying low mobilities of charge carriers. (BFCO is not shown in this figure because its effective mass is larger than $8m_e$.)[13] On the other hand, several ferroelectric semiconductors such as $ABiO_3$ (A = Mg, Zn, Cd, and Ca)[41] and $ZnSnS_3$[42] (purple circles) were theoretically suggested for PV applications. They have relatively small band gaps and moderate effective masses, but they are outperformed by Ba_4Pn_2O. Furthermore, they have not been synthesized in experiments yet, while Ba_4Pn_2O already exist.

4. CONCLUSIONS

In conclusion, we theoretically confirmed that antiperovskite Ba_4Pn_2O (Pn = As and Sb) is a promising ferroelectric semiconductor for PVs. We have shown that the displacement of O^{2-} and axial Ba^{4+} ions in the opposite direction along the *c*-axis results in ferroelectricity in Ba_4Pn_2O. In addition, we have demonstrated that the direct nature and optimal band gap of Ba_4Pn_2O will allow for significant absorption of visible light such that thin layers of Ba_4Pn_2O would be able to yield low-cost and high-efficiency solar cells. Unlike most of ferroelectric oxides, Ba_4Pn_2O is found to have the small effective masses of charge carriers, implying facile extraction of photocarriers. In light of the favorable simulation results and confirmed synthesizability, we believe that Ba_4Pn_2O can pave a new avenue for the development of next-generation PVs.

■ ASSOCIATED CONTENT

Supporting Information

The Supporting Information is available free of charge at https://pubs.acs.org/doi/10.1021/acsami.0c13034.

Convergence test for *GW* calculations, possible crystal structures of Ba_4As_2O, anisotropy in absorption coefficients of Ba_4Pn_2O, atom-resolved partial density of states of Ba_4Pn_2O, and PBE + SOC calculation results using different computational parameters (PDF)

■ AUTHOR INFORMATION

Corresponding Author

Youngho Kang – *Department of Materials Science and Engineering, Incheon National University, Incheon 22012, Korea;* orcid.org/0000-0003-4532-0027; Email: youngho84@inu.ac.kr

Author

Seungwu Han – *Department of Materials Science and Engineering, Seoul National University, Seoul 08826, Korea;* orcid.org/0000-0003-3958-0922

Complete contact information is available at: https://pubs.acs.org/10.1021/acsami.0c13034

Notes

The authors declare no competing financial interest.

■ ACKNOWLEDGMENTS

This work was supported by the Creative Materials Discovery Program (RIAM) through the National Research Foundation of Korea (NRF) funded by the Ministry of Science and ICT (2017M3D1A1040689).

■ REFERENCES

(1) Röhm, H.; Leonhard, T.; Schulz, A. D.; Wagner, S.; Hoffmann, M. J.; Colsmann, A. Ferroelectric Properties of Perovskite Thin Films and Their Implications for Solar Energy Conversion. *Adv. Mater.* **2019**, *31*, 1806661.

(2) Nechache, R.; Harnagea, C.; Li, S.; Cardenas, L.; Huang, W.; Chakrabartty, J.; Rosei, F. Bandgap Tuning of Multiferroic Oxide Solar Cells. *Nat. Photonics* **2014**, *9*, 61−67.
(3) Paillard, C.; Bai, X.; Infante, I. C.; Guennou, M.; Geneste, G.; Alexe, M.; Kreisel, J.; Dkhil, B. Photovoltaics with Ferroelectrics: Current Status and Beyond. *Adv. Mater.* **2016**, *28*, 5153−5168.
(4) Wu, L.; Podpirka, A.; Spanier, J. E.; Davies, P. K. Ferroelectric, Optical, and Photovoltaic Properties of Morphotropic Phase Boundary Compositions in the $PbTiO_3$−$BiFeO_3$−$Bi(Ni_{1/2}Ti_{1/2})O_3$ System. *Chem. Mater.* **2019**, *31*, 4184−4194.
(5) Sando, D.; Carrétéro, C.; Grisolia, M. N.; Barthélémy, A.; Nagarajan, V.; Bibes, M. Revisiting the Optical Band Gap in Epitaxial $BiFeO_3$ Thin Films. *Adv. Opt. Mater.* **2018**, *6*, 1700836.
(6) Suzuki, K.; Kijima, K. Optical Band Gap of Barium Titanate Nanoparticles Prepared by RF-Plasma Chemical Vapor Deposition. *Jpn. J. Appl. Phys.* **2005**, *44*, 2081−2082.
(7) Tiwari, R. P.; Birajdar, B.; Ghosh, R. K. Strain Engineering of Ferroelectric $KNbO_3$ for Bulk Photovoltaic Applications: An Insight from Density Functional Theory Calculations. *J. Phys.: Condens. Matter* **2019**, *31*, 505502.
(8) Chen, G.; Chen, J.; Pei, W.; Lu, Y.; Zhang, Q.; Zhang, Q.; He, Y. Bismuth Ferrite Materials for Solar Cells: Current Status and Prospects. *Mater. Res. Bull.* **2019**, *110*, 39−49.
(9) Ji, W.; Yao, K.; Liang, Y. C. Bulk Photovoltaic Effect at Visible Wavelength in Epitaxial Ferroelectric $BiFeO_3$ Thin Films. *Adv. Mater.* **2010**, *22*, 1763−1766.
(10) Grinberg, I.; West, D. V.; Torres, M.; Gou, G.; Stein, D. M.; Wu, L.; Chen, G.; Gallo, E. M.; Akbashev, A. R.; Davies, P. K.; Spanier, J. E.; Rappe, A. M. Perovskite Oxides for Visible-Light-Absorbing Ferroelectric and Photovoltaic Materials. *Nature* **2013**, *503*, 509−512.
(11) Han, H.; Song, S.; Lee, J. H.; Kim, K. J.; Kim, G.-W.; Park, T.; Jang, H. M. Switchable Photovoltaic Effects in Hexagonal Manganite Thin Films Having Narrow Band Gaps. *Chem. Mater.* **2015**, *27*, 7425−7432.
(12) Song, S.; Kim, D.; Jang, H. M.; Yeo, B. C.; Han, S. S.; Kim, C. S.; Scott, J. F. β-$CuGaO_2$ as a Strong Candidate Material for Efficient Ferroelectric Photovoltaics. *Chem. Mater.* **2017**, *29*, 7596−7603.
(13) Kim, D.; Han, H.; Lee, J. H.; Choi, J. W.; Grossman, J. C.; Jang, H. M.; Kim, D. Electron−hole Separation in Ferroelectric Oxides for Efficient Photovoltaic Responses. *Proc. Natl. Acad. Sci. U. S. A.* **2018**, *115*, 6566−6571.
(14) Frost, J. M.; Butler, K. T.; Brivio, F.; Hendon, C. H.; Van Schilfgaarde, M.; Walsh, A. Atomistic Origins of High-Performance in Hybrid Halide Perovskite Solar Cells. *Nano Lett.* **2014**, *14*, 2584−2590.
(15) Butler, K. T.; Frost, J. M.; Walsh, A. Ferroelectric Materials for Solar Energy Conversion: Photoferroics Revisited. *Energy Environ. Sci.* **2015**, *8*, 838−848.
(16) Green, M. A.; Dunlop, E. D.; Hohl-Ebinger, J.; Yoshita, M.; Kopidakis, N.; Ho-Baillie, A. W. Y. Solar Cell Efficiency Tables (Version 55). *Prog. Photovolt: Res. Appl.* **2020**, *28*, 3−15.
(17) Polman, A.; Knight, M.; Garnett, E. C.; Ehrler, B.; Sinke, W. C. Photovoltaic Materials: Present Efficiencies and Future Challenges. *Science* **2016**, *352*, aad4424.
(18) Leijtens, T.; Eperon, G. E.; Noel, N. K.; Habisreutinger, S. N.; Petrozza, A.; Snaith, H. J. Stability of Metal Halide Perovskite Solar Cells. *Adv. Energy Mater.* **2015**, *5*, 1500963.
(19) Kang, Y.; Youn, Y.; Han, S.; Park, J.; Oh, C.-S. Computational Screening of Indirect-Gap Semiconductors for Potential Photovoltaic Absorbers. *Chem. Mater.* **2019**, *31*, 4072−4080.
(20) Fabini, D. H.; Koerner, M.; Seshadri, R. Candidate Inorganic Photovoltaic Materials from Electronic Structure-Based Optical Absorption and Charge Transport Proxies. *Chem. Mater.* **2019**, *31*, 1561−1574.
(21) Shockley, W.; Queisser, H. J. Detailed Balance Limit of Efficiency of p-n Junction Solar Cells. *J. Appl. Phys.* **1961**, *32*, 510−519.
(22) Kresse, G.; Furthmüller, J. Efficient Iterative Schemes for Ab Initio Total-Energy Calculations Using a Plane-Wave Basis Set. *Phys. Rev. B* **1996**, *54*, 11169.
(23) Kresse, G.; Joubert, D. From Ultrasoft Pseudopotentials to the Projector Augmented-Wave Method. *Phys. Rev. B* **1999**, *59*, 1758.
(24) Tadano, T.; Gohda, Y.; Tsuneyuki, S. Anharmonic Force Constants Extracted from First-Principles Molecular Dynamics: Applications to Heat Transfer Simulations. *J. Phys.: Condens. Matter* **2014**, *26*, 225402.
(25) Tadano, T.; Tsuneyuki, S. Self-Consistent Phonon Calculations of Lattice Dynamical Properties in Cubic $SrTiO_3$ with First-Principles Anharmonic Force Constants. *Phys. Rev. B* **2015**, *92*, 054301.
(26) Perdew, J. P.; Burke, K.; Ernzerhof, M. Generalized Gradient Approximation Made Simple. *Phys. Rev. Lett.* **1996**, *77*, 3865.
(27) Del Sole, R.; Girlanda, R. Optical Properties of Semiconductors within the Independent-Quasiparticle Approximation. *Phys. Rev. B* **1993**, *48*, 11789.
(28) Debbichi, L.; Lee, S.; Cho, H.; Rappe, A. M.; Hong, K.-H.; Jang, M. S.; Kim, H. Mixed Valence Perovskite $Cs_2Au_2I_6$: A Potential Material for Thin-Film Pb-Free Photovoltaic Cells with Ultrahigh Efficiency. *Adv. Mater.* **2018**, *30*, 1707001.
(29) Röhr, C.; George, R. Crystal Structure of Barium Antimonide Oxide, Ba4Sb2O. *Z. Kristallogr.* **1996**, *211*, 478.
(30) Artini, C.; Carnasciali, M. M.; Costa, G. A.; Magnone, E.; Mele, P. Search for New Superconducting Oxides in M_4Pn_2O Phases (M = Ca, Sr, Ba and Pn = As, Sb, Bi). *Physica C* **2002**, *372*−*376*, 1266−1269.
(31) Marronnier, A.; Lee, H.; Geffroy, B.; Even, J.; Bonnassieux, Y.; Roma, G. Structural Instabilities Related to Highly Anharmonic Phonons in Halide Perovskites. *J. Phys. Chem. Lett.* **2017**, *8*, 2659−2665.
(32) Porter, S. H.; Huang, Z.; Woodward, P. M. Study of Anion Order/Disorder in $RTaN_2O$ (R = La, Ce, Pr) Perovskite Nitride Oxides. *Cryst. Growth Des.* **2014**, *14*, 117−125.
(33) Perdew, J. P.; Ruzsinszky, A.; Csonka, G. I.; Vydrov, O. A.; Scuseria, G. E.; Constantin, L. A.; Zhou, X.; Burke, K. Restoring the Density-Gradient Expansion for Exchange in Solids and Surfaces. *Phys. Rev. Lett.* **2008**, *100*, 136406.
(34) Kang, Y.; Kang, G.; Nahm, H. H.; Cho, S. H.; Park, Y. S.; Han, S. G. W. Calculations on Post-Transition-Metal Oxides. *Phys. Rev. B* **2014**, *89*, 165130.
(35) Shishkin, M.; Kresse, G. Self-Consistent GW Calculations for Semiconductors and Insulators. *Phys. Rev. B* **2007**, *75*, 235102.
(36) Ziang, X.; Shifeng, L.; Laixiang, Q.; Shuping, P.; Wei, W.; Yu, Y.; Li, Y.; Zhijian, C.; Shufeng, W.; Honglin, D.; Minghui, Y.; Qin, G. G. Refractive Index and Extinction Coefficient of $CH_3NH_3PbI_3$ Studied by Spectroscopic Ellipsometry. *Opt. Mater. Express* **2015**, *5*, 29−43.
(37) Heyd, J.; Scuseria, G. E.; Ernzerhof, M. Hybrid Functionals Based on a Screened Coulomb Potential. *J. Chem. Phys.* **2003**, *118*, 8207−8215.
(38) Heyd, J.; Scuseria, G. E.; Ernzerhof, M. Erratum: Hybrid Functionals Based on a Screened Coulomb Potential (Journal of Chemical Physics (2003) 118 (8207)). *J. Chem. Phys.* **2006**, *124*, 219906.
(39) Kang, Y.; Han, S. Intrinsic Carrier Mobility of Cesium Lead Halide Perovskites. *Phys. Rev. Appl.* **2018**, *10*, 044103.
(40) Krishnaswamy, K.; Himmetoglu, B.; Kang, Y.; Janotti, A.; Van De Walle, C. G. First-Principles Analysis of Electron Transport in $BaSnO_3$. *Phys. Rev. B* **2017**, *95*, 205202.
(41) He, J.; Franchini, C.; Rondinelli, J. M. Ferroelectric Oxides with Strong Visible-Light Absorption from Charge Ordering. *Chem. Mater.* **2017**, *29*, 2445−2451.
(42) Kolb, B.; Kolpak, A. M. First-Principles Design and Analysis of an Efficient, Pb-Free Ferroelectric Photovoltaic Absorber Derived from $ZnSnO_3$. *Chem. Mater.* **2015**, *27*, 5899−5906.
(43) Suzuki, I.; Nagatani, H.; Kita, M.; Iguchi, Y.; Sato, C.; Yanagi, H.; Ohashi, N.; Omata, T. First Principles Calculations of Ternary Wurtzite β-$CuGaO_2$. *J. Appl. Phys.* **2016**, *119*, 095701.

https://dx.doi.org/10.1021/acsami.0c13034
ACS Appl. Mater. Interfaces 2020, 12, 43798−43804

(44) Shenton, J. K.; Bowler, D. R.; Cheah, W. L. Influence of Crystal Structure on Charge Carrier Effective Masses in $BiFeO_3$. *Phys. Rev. B* **2019**, *100*, 085120.
(45) Xu, Y.-Q.; Wu, S.-Y.; Ding, C.-C.; Wu, L.-N.; Zhang, G.-J. First-Principles Investigation on the Mechanism of Photocatalytic Properties for Cubic and Orthorhombic $KNbO_3$. *Chem. Phys.* **2018**, *504*, 66−71.
(46) Yang, F.; Lin, S.; Yang, L.; Liao, J.; Chen, Y.; Wang, C.-Z. First-Principles Investigation of Metal-Doped Cubic $BaTiO_3$. *Mater. Res. Bull.* **2017**, *96*, 372−378.
(47) Li, Y.; Singh, D. J. Properties of the ferroelectric visible light absorbing semiconductors: $Sn_2P_2S_6$ and $Sn_2P_2Se_6$. *Phys. Rev. Mater.* **2017**, *1*, 075402.

https://dx.doi.org/10.1021/acsami.0c13034
ACS Appl. Mater. Interfaces 2020, 12, 43798−43804